Secondary breakup of axisymmetric liquid drops. II. Impulsive acceleration

Jaehoon Han[a] and Grétar Tryggvason[b]
Mechanical Engineering and Applied Mechanics, The University of Michigan, Ann Arbor, Michigan 48109-2121

(Received 3 April 2000; accepted 15 March 2001)

The secondary breakup of impulsively accelerated liquid drops is examined for small density differences between the drops and the ambient fluid. Two cases are examined in detail: a density ratio close to unity and a density ratio of 10. A finite difference/front tracking numerical technique is used to solve the unsteady axisymmetric Navier–Stokes equations for both the drops and the ambient fluid. The breakup is governed by the Weber number, the Reynolds number, the viscosity ratio, and the density ratio. The results show that Weber number effects are dominant. In the higher density ratio case, $\rho_d/\rho_o=10$, different breakup modes—oscillatory deformation, backward-facing bag mode, and forward-facing bag mode—are seen as the Weber number increases. The forward-facing bag mode observed at high Weber numbers is an essentially inviscid phenomenon, as confirmed by comparisons with inviscid flow simulations. At the lower density ratio, $\rho_d/\rho_o=1.15$, the backward-facing bag mode is absent. The deformation rate also becomes larger as the Weber number increases. The Reynolds number has a secondary effect, changing the critical Weber numbers for the transitions between breakup modes. The increase of the drop viscosity reduces the drop deformation. The results are summarized by ''breakup maps'' where the different breakup modes are shown in the We–Re plane for different values of the density ratios. © *2001 American Institute of Physics.* [DOI: 10.1063/1.1370389]

I. INTRODUCTION

In spray combustion, secondary atomization of liquid droplets plays an important role in the increase of surface area and the enhancement of heat and mass transfer between the fuel and the ambient gas. In part I,[1] we discussed the secondary breakup of liquid drops that are accelerated by a constant body force. The Eötvös number, which is the ratio of the body force to the surface tension, was found to be the main controlling parameter. The fluid viscosities and the density ratio had secondary effects. Here, we investigate another type of disturbance causing drop breakup: impulsive acceleration of the droplet. This corresponds to an experimental situation where a liquid droplet is accelerated by a shock wave. This type of disturbance has been employed in many experimental studies of secondary breakup. Earlier studies include Lane;[2] Hinze;[3] Hanson *et al.*;[4] Ranger and Nicholls;[5] and Gel'fand *et al.*[6] For more recent studies of liquid atomization, see Krzeczkowski;[7] Borisov *et al.*;[8] Reitz and Bracco;[9] Pilch and Erdman;[10] Wierzba;[11] Hsiang and Faeth;[12–14] and Joseph *et al.*[15] Comprehensive reviews of studies on the secondary breakup are provided by Gel'fand[16] and Liu.[17]

Experimental results are usually presented in terms of four nondimensional numbers: the Weber number We, the Reynolds number Re, the density ratio, and the viscosity ratio. The Reynolds number is sometimes replaced by the Ohnesorge number Oh. These numbers are defined later in this article. The experimental data show that the breakup of drops in gas flows can generally be categorized into four different modes:[18]

(1) Vibrational breakup mode where the original drop disintegrates into two or four equal-sized smaller drops.
(2) Bag breakup mode where the original drop deforms into a torus-shaped rim spanned by a thin fluid film that ruptures into tiny droplets, followed by the disintegration of the rim into larger droplets. Sometimes, a tiny streamer is also formed inside the bag, called the parachute or the umbrella breakup mode.
(3) Shear breakup mode where continuous stripping of fluid from the drop surface occurs.
(4) Explosive breakup mode where the drop disintegrates in a violent manner due to strong surface waves.

In modes 2 and 3, the breakup process is initiated by the axisymmetric flattening of the drop into an ellipsoid or disk shape. For modes 1 and 4, the formation of a disk is not seen and there are good reasons to believe that the breakup is fully three-dimensional from the start. In some experiments, a transitional mode is seen between modes 2 and 3, where the drop breaks up due to both the formation of a bag and the stripping of fluid from the drop surface. This categorization and terminology are somewhat arbitrary and different variations have been suggested by different researchers. For example, the umbrella breakup mode has also been called ''bag-jet mechanism''[7] and ''bag-and-stamen breakup.''[10]

The transitions between the breakup modes described above take place at critical Weber numbers that generally depend only weakly on the Ohnesorge number based on drop

[a]Present address: AVL Powertrain Engineering Inc., 47519 Halyard Drive, Plymouth, MI 48170-2438; telephone: (877) 285-4278; fax: (734) 414-9690; electronic mail: jaehoon.han@avlna.com
[b]Present address: Mechanical Engineering Department, 100 Institute Road, Worcester Polytechnic Institute, Worcester, MA 01609-2280; telephone: (508) 831-5759; fax: (508) 831-5680; electronic mail: gretar@wpi.edu

 © 2001 American Institute of Physics

properties. For low viscosity drops, the critical Weber numbers are approximately 10, 20–60, and 1000, respectively, for the transitions from one mode to the next one. It is also found that the critical Weber numbers increase as the Ohnesorge number increases. Note that the first three breakup modes are realized for a very narrow range of Weber numbers. Wierzba[11] found that in the range of $11 \leqslant We \leqslant 14$, the drop deformation and the breakup are very sensitive to small fluctuations of the experimental conditions and he could further refine the observed breakup into five subcategories. There are large variations in the critical Weber numbers in the available experimental data due to different test conditions. Thus the numbers presented above should be considered only as a rough guide.

Most previous studies have been done for liquid–gas systems at atmospheric pressure and temperature. The behavior of liquid droplets at smaller density ratios (a characteristic of high pressure combustion systems) is not well-understood yet.[16] In this study, computational results are presented for impulsively started drops in which the motion and the deformation of the drop are caused by the initial momentum due to a step-change in the relative velocity. Numerical simulations have been done for two density ratios, 1.15 and 10. These values are in the range of typical density ratios encountered in practical spray combustion systems [density ratios of $O(10)$ for diesel engines[19] and $O(1)$ for rocket motors are common]. As discussed in part I, simulations in the Boussinesq limit using the smaller density ratio, 1.15, can be scaled to predict the drop behavior at other density ratios close to 1. The effects of the individual governing parameters are examined and the physical mechanisms associated with different breakup modes are discussed.

II. FORMULATION AND NUMERICAL METHOD

A. Navier–Stokes equations

The physical problem and the computational domain are sketched in Fig. 1. The domain is axisymmetric and the left boundary is the axis of symmetry. At the start of the computation ($t=0$), the drop is spherical and given an impulsive motion downward due to a step change in the relative velocity. (If coordinates fixed at the drop centroid are adopted, the incoming ambient fluid flow moves upward.) We solve for the flow everywhere, both inside and outside the drop. The Navier–Stokes equations are valid for both fluids, and a single set of equations can be written for the whole domain as long as the jump in density and viscosity is correctly accounted for and surface tension is included.

The Navier–Stokes equations in conservative form are

$$\frac{\partial \rho \mathbf{u}}{\partial t} + \nabla \cdot (\rho \mathbf{u}\mathbf{u}) = -\nabla p + \nabla \cdot \mu(\nabla \mathbf{u} + \nabla^T \mathbf{u}) + \sigma \int_S \kappa \mathbf{n} \delta(\mathbf{x} - \mathbf{x}_f)\, dS, \tag{1}$$

where $\mathbf{u}$ is the velocity, p is the pressure, and ρ and μ are the discontinuous density and viscosity fields, respectively. The effect of surface tension is included as a singular body force in the final term, where σ is the surface tension, κ is twice the mean curvature, and $\mathbf{n}$ is a unit vector normal to the interface. The contribution of the surface tension is limited to the interface itself, as indicated by the three-dimensional delta function, δ. In the argument of δ, $\mathbf{x}$ is the point at which the equation is evaluated, and $\mathbf{x}_f$ is a point at the interface. The integral over the surface of the drop, S, results in a force distribution that is smooth and continuous along the drop surface.

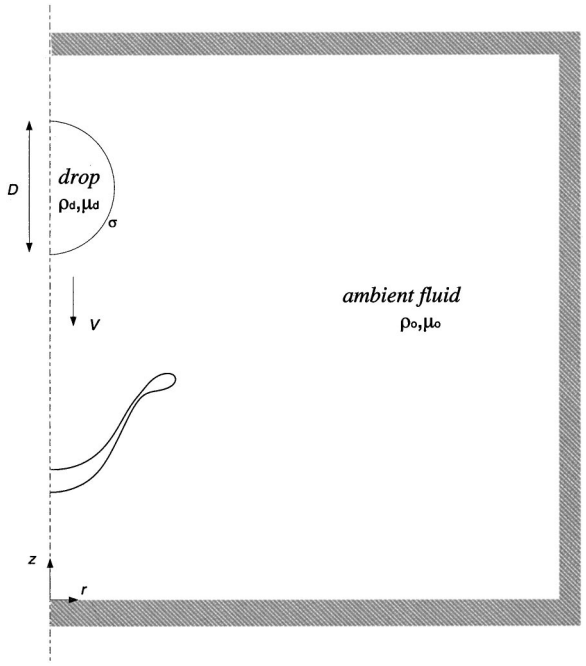

FIG. 1. Schematic diagram of the computational domain.

The above equations are supplemented by the incompressibility condition:

$$\nabla \cdot \mathbf{u} = 0, \tag{2}$$

and equations of state for the physical properties:

$$\frac{D\rho}{Dt} = 0; \quad \frac{D\mu}{Dt} = 0, \tag{3}$$

where D/Dt is the total derivative. These two equations simply state that the physical properties of each fluid remain constant in the case of immiscible fluids.

Dimensional analysis shows that a set of four independent dimensionless parameters can be constructed for the dynamics of drop deformation and breakup. When the drop is subject to an impulsive acceleration, it is convenient to choose the Weber number We; the Reynolds number based on the ambient fluid properties Re; the density ratio; and the viscosity ratio. These are defined by

$$\mathrm{We} = \frac{\rho_o V^2 D}{\sigma}; \quad \mathrm{Re} = \frac{\rho_o V D}{\mu_o}; \quad \frac{\rho_d}{\rho_o}; \quad \frac{\mu_d}{\mu_o}. \tag{4}$$

Sometimes, the viscosity ratio is replaced by the drop Reynolds number, $\mathrm{Re}_d = \rho_d V D/\mu_d$. Here, D is the initial diameter of the drop and V is the initial relative velocity between the drop and the ambient fluid. The subscripts, d and o, denote the properties of the drop and the ambient fluid, respectively.

Another parameter often used in the literature is the Ohnesorge number, $\mathrm{Oh}=\mu/\sqrt{\rho D\sigma}=\sqrt{\mathrm{We}}/\mathrm{Re}$, which is the ratio of the viscous shear to the surface tension.

The momentum equations and the continuity equation are discretized using an explicit second-order predictor-corrector time-integration method combined with a second-order centered difference method for the spatial derivatives. The discretized equations are solved on a fixed, staggered grid. The grid spacing is non-uniform in order to improve the accuracy of the computation in some specific regions. For simulations with $\rho_d/\rho_o=1.15$, a fixed computational domain is used and the full-slip boundary condition, where both the normal component and the gradient of the tangential component of the velocity are zero, is applied to all four boundaries. For the $\rho_d/\rho_o=10$ simulations, where the drops move a longer distance, a reference frame moving with the centroid of the drop is employed. The motion of the domain is determined from the solution and an extra acceleration term is added to the governing equation to account for the time-dependent motion of the domain. The boundary conditions have also been modified to include a constant flow at the bottom and a zero velocity gradient in the normal direction at the top. The use of moving coordinates has been shown in part I to be very effective in keeping the computational cost reasonable while maintaining the necessary resolution around the moving drop.

In order to accurately simulate a highly deformed interface during breakup, a front-tracking method is employed, where the interface is represented by marker points that are moved by interpolating their velocities from the stationary grid. These points are connected to form a ''front'' which is used to construct the property fields at each time step. This front is also used to calculate the surface tension. Throughout the computation, the front points are dynamically added and deleted to avoid excessive stretching or clustering of neighboring front points. This ensures that there exist approximately two to five front points per fixed grid spacing. For a more detailed description of the front tracking method, see Refs. 20 and 21.

The numerical method described earlier is essentially the same as in the constant acceleration case presented in part I. The only difference in terms of numerical procedures exists in the initial flow condition. In shock tube experiments, the main function of the shock is to produce a high-speed convective flow, while the collision between the shock and the droplet has little effect on the breakup phenomenon.[17] In our numerical simulations, this initial flow field is calculated as follows: We estimate the vorticity distribution at $t=0$ on the drop interface based on the inviscid flow solution for a spherical drop moving with a velocity V. Then, the vorticity is distributed to the neighboring fixed grid points and the corresponding velocity field is obtained by solving the Poisson equation for the stream function, $\nabla^2\psi=-\omega$.

The majority of the simulations presented here were carried out on HP 9000 workstations. A typical run generally required between 4000 and 120 000 time-steps and took 12–240 h, depending on the parameters of the problem.

B. Inviscid flow

To address to what extent the drop evolution can be described by an inviscid model, a few simulations were done using a vortex method. The interface separating the drop and the ambient fluid is a vortex sheet, and an evolution equation for the vortex sheet strength $\gamma=(\mathbf{u}_d-\mathbf{u}_o)\cdot\mathbf{s}$ can be derived by subtracting the tangential components of the Euler equations on either side of the interface. The resulting equation is (see, for example, Ref. 22)

$$\frac{D\gamma}{Dt}+\gamma\frac{\partial\mathbf{U}}{\partial s}\cdot\mathbf{s}=2\mathrm{A}\left(\frac{D\mathbf{U}}{Dt}\cdot\mathbf{s}+\frac{1}{8}\frac{\partial\gamma^2}{\partial s}\right)-\frac{\sigma}{\rho_d+\rho_o}\frac{\partial\kappa}{\partial s}. \quad (5)$$

Here, $\mathrm{A}=(\rho_d-\rho_o)/(\rho_d+\rho_o)$ is the Atwood number, $\mathbf{U}=(\mathbf{u}_d+\mathbf{u}_o)/2$ is the average of the velocities on either side of the vortex sheet, and κ is the mean curvature. Given the vortex sheet strength γ, the velocity is found by the Biot–Savart integral. For computational purposes, the axisymmetric vortex sheet is discretized by a finite number of vortex rings. The azimuthal integration can be done analytically and the integral is therefore replaced by a summation over the discrete vortex rings. The radial and axial velocities at a point on ring j are given by

$$u_j=\frac{1}{\pi}\sum_{l=1}^{N}\frac{\Gamma_l r_l k_{lj}(z_j-z_l)}{(4r_j r_l)^{3/2}}\left[\left(\frac{k_{lj}^2-2}{1-k_{lj}^2}\right)E(k_{lj})+2K(k_{lj})\right], \quad (6)$$

$$v_j=\frac{1}{\pi}\sum_{l=1}^{N}\frac{\Gamma_l r_l k_{lj}}{(4r_j r_l)^{3/2}}\times\left[\left(\frac{(r_l+r_j)k_{lj}^2-2r_l}{1-k_{lj}^2}\right)E(k_{lj})+2r_l K(k_{lj})\right]. \quad (7)$$

Here, Γ is the circulation, $K(k)$ is the complete elliptic integral of the first kind, $E(k)$ is the complete elliptic integral of the second kind, and

$$k_{lj}=\frac{2\sqrt{r_l r_j}}{\sqrt{(r_l+r_j)^2+(z_j-z_l)^2}}. \quad (8)$$

The elliptic integrals can be computed efficiently by a polynomial approximation.[23] When the axisymmetric vortex sheet is replaced by discrete vortex rings, the rings must be given a finite core size to avoid infinite self-induced velocity. This can be accomplished simply by replacing k_{lj} by

$$\tilde{k}_{lj}=\frac{2\sqrt{r_l r_j}}{\sqrt{(r_l+r_j)^2+(z_j-z_l)^2+\delta^2}}, \quad (9)$$

where δ is a small regularization parameter. In the limit of $N\to\infty$ and $\delta\to 0$ the solution will be independent of the exact value of δ (except at isolated points where roll-up takes place).

The evolution equation for the circulation of each vortex ring can be obtained by integrating Eq. (5) over a small material segment:

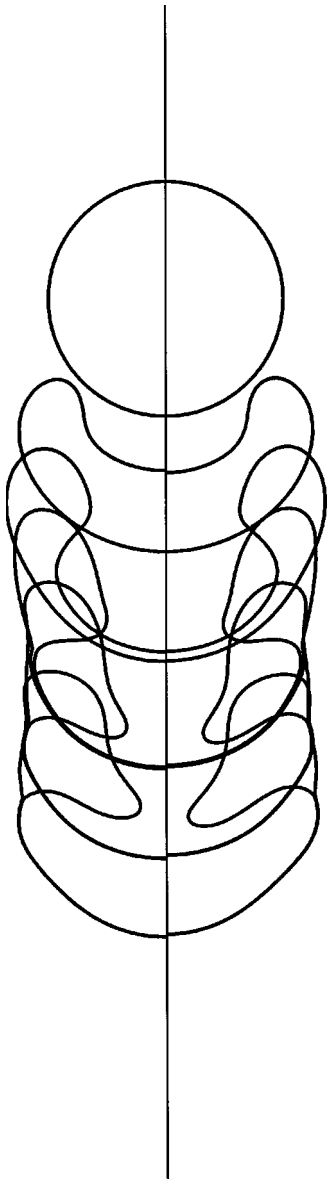

FIG. 2. Grid refinement test. The breakup of a impulsively started drop computed using a 128×256 grid (left) and a 256×512 grid (right). $\rho_d/\rho_o=1.15$, We=54.7, Re=331, Re_d=381. The drop shape is plotted every $\Delta t_p^*=0.909$.

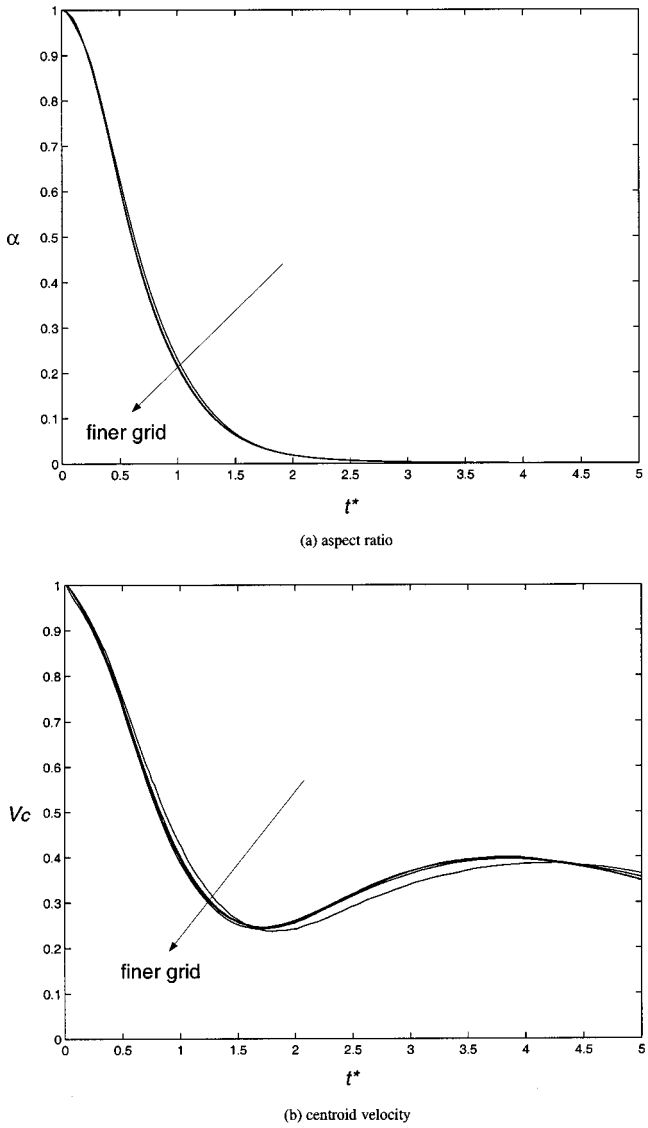

FIG. 3. Grid refinement test. Aspect ratio and centroid velocity plotted vs t^*. Results using four different grids, 64×128, 128×256, 256×512, and 512×1024 are shown. $\rho_d/\rho_o=1.15$, We=54.7, Re=331, Re_d=381.

$$\frac{D\Gamma}{Dt}=2A\int_{s(\alpha^-)}^{s(\alpha^+)}\left[\frac{D\mathbf{U}}{Dt}\cdot\mathbf{s}+\frac{1}{8}\frac{\partial\gamma^2}{\partial s}\right]ds - \frac{\sigma}{\rho_d+\rho_o}[\kappa(\alpha^+)-\kappa(\alpha^-)], \tag{10}$$

where α^+ and α^- are the two end points of the segment. Equation (10), along with the equation $D\mathbf{x}/Dt=\mathbf{U}$, where $\mathbf{x}=(r,z)$ is the position vector for each vortex ring, can be integrated using a time-integration method such as the fourth-order Runge–Kutta method once the initial vorticity distribution and the geometry are given. The $D\mathbf{U}/Dt$ term is found in an iterative manner: First the interface is advanced and the circulations are updated using $D\mathbf{U}/Dt$ from last time-step as an approximation. Then the velocities at the new position are found using the approximate values of the circulations. The velocities are then used to calculate $D\mathbf{U}/Dt$ at the original interface position and the process is repeated.

III. RESULTS AND DISCUSSION

Most of the simulations presented here are for $\rho_d/\rho_o=10$. The effects of the Weber number, the Reynolds number, and the viscosity ratio are studied. In addition, a few simulations have been done for $\rho_d/\rho_o=1.15$ to examine the effect of the density ratio. As discussed in part I, the Boussinesq approximation applies when the drop and the ambient fluid have similar densities. Thus a single simulation with one specific value of the density ratio close to 1 can be rescaled for a range of density ratios. When presenting the results, time is nondimensionalized with the diameter and the initial relative velocity, $t^*=tV/D$.

In order to validate the numerical method, grid refinement tests were done and one case is shown in Fig. 2 for

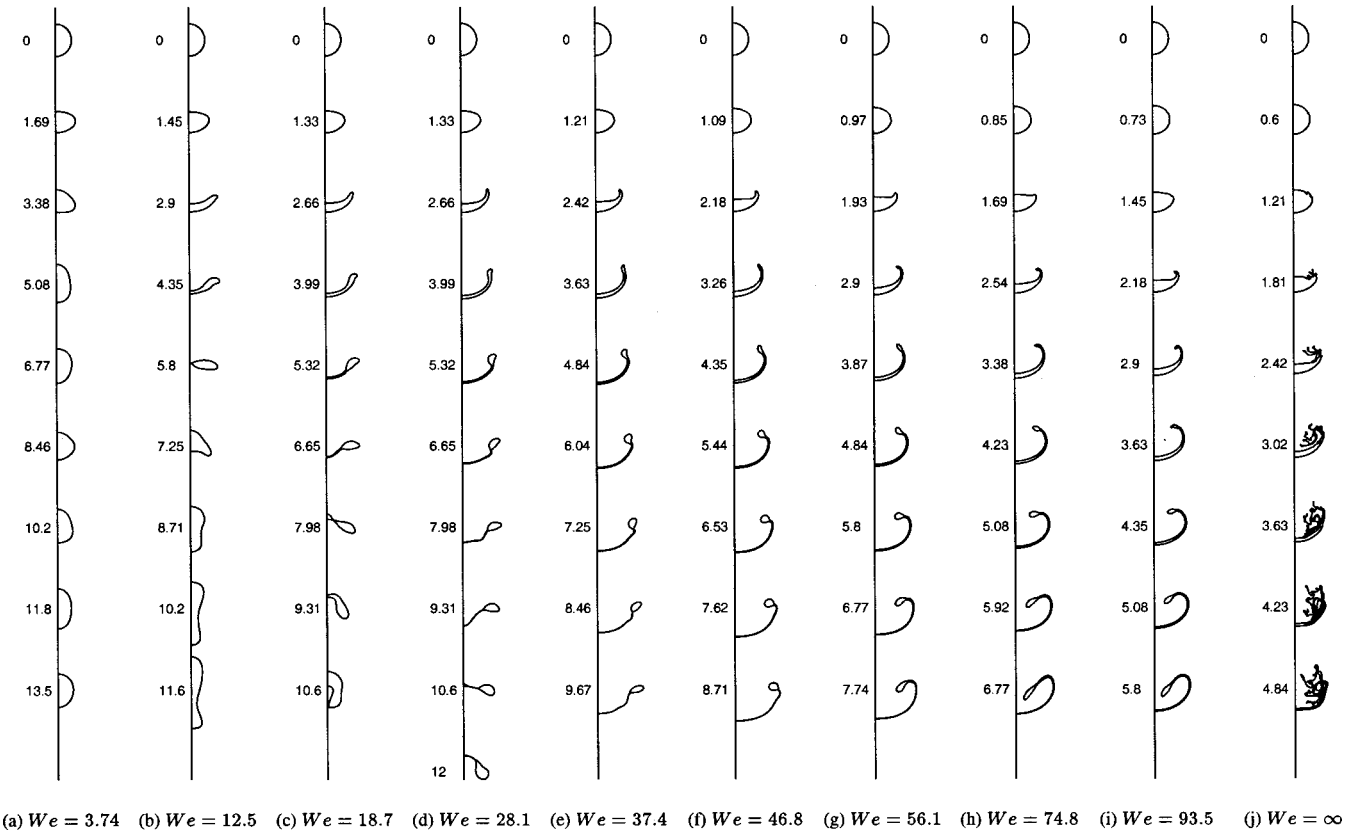

FIG. 4. Effect of We on the deformation of impulsively started drops with $\rho_d/\rho_o = 10$, Re=242, and $\mathrm{Re}_d = 1935$. The numbers next to the drops denote t^* when the drop contours are plotted. The centroids of the drops in a column are separated by a fixed distance. The gap between two successive drops in a column does not represent the distance the drop travels during the time interval. The computations were done on a 256×512 grid.

$\rho_d/\rho_o = 1.15$, We=54.7, Re=331, and $\mathrm{Re}_d = 381$. The computational domain has a dimension of 2.5 and 5 times the initial drop diameter in the radial and axial directions, respectively, and is resolved by two different grids: 128×256 (left) and 256×512 (right). The shape of the drop is plotted at time intervals $\Delta t_p^* = 0.909$. The results agree well, despite the large deformation of the drop. In Fig. 3, the aspect ratio and the centroid velocity are plotted versus t^* for the cases shown in Fig. 2 and two other simulations done using a 64×128 and a 512×1024 grids. The aspect ratio is defined as the drop thickness at the centerline divided by the maximum width of the drop. The centroid velocity of the drop is found by taking the volume average of the vertical velocity inside the drop. The result for the 64×128 grid shows a small difference but the results with the three finer grids are nearly identical.

A. Effect of We at a fixed Re

1. Evolution of drops with $\rho_d/\rho_o = 10$

In Fig. 4, the deformation and breakup of drops with $\rho_d/\rho_o = 10$ are shown for Re=242 and $\mathrm{Re}_d = 1935$. Results for We=3.74, 12.5, 18.7, 28.1, 37.4, 46.8, 56.1, 74.8, 93.5, and ∞ are compared. For these parameters (excluding the We=∞ case), the ranges of the Ohnesorge numbers are 0.008–0.04 and 0.0032–0.0158 for the ambient fluid and the drop, respectively. Experimental evidence suggests that when Oh$<$0.1, the viscosity has only minor effects and that surface tension effects are dominant. The computational domain has a dimension of 2.5 and 5 times the initial drop diameter in the radial and axial directions, respectively, and is resolved by a 256×512 grid. The grid is slightly stretched and the average number of grid points across the drop diameter is between 100 and 180, depending on how deformed the drop is.

The drop in (a) with We=3.74 shows oscillatory deformation. The drops with We=12.5 and 18.7 in (b) and (c) initially develop an indentation on the side facing the downstream of the incoming ambient fluid flow (the side facing upward in the figures) and it continues to deepen. As the deformations increase the drag, the initial momentum of the drop fluid decreases. This reduces the aerodynamic pressure variations around the drop and the influence of the surface tension starts to increase. At later stages of the deformation, the We=12.5 drop displays oscillatory deformation while the We=18.7 drop shows the formation of a backward-facing bag (a thin hollow bag facing the downstream direction is attached to a toroidal rim) at $t^* = 7.98$. Eventually, the backward-facing bag in (c) stops growing and the drop restores its original spherical shapes. The drop shown in (d) for We=28.1 shows the formation of a backward-facing bag more clearly at $t^* = 12$. The Weber numbers for the drops in (b)–(d) are in the range where a bag breakup mode is observed experimentally for higher density ratios. The results in (e)–(i), for even higher Weber numbers, show, on the other hand, the formation of a forward-facing bag (the bag is

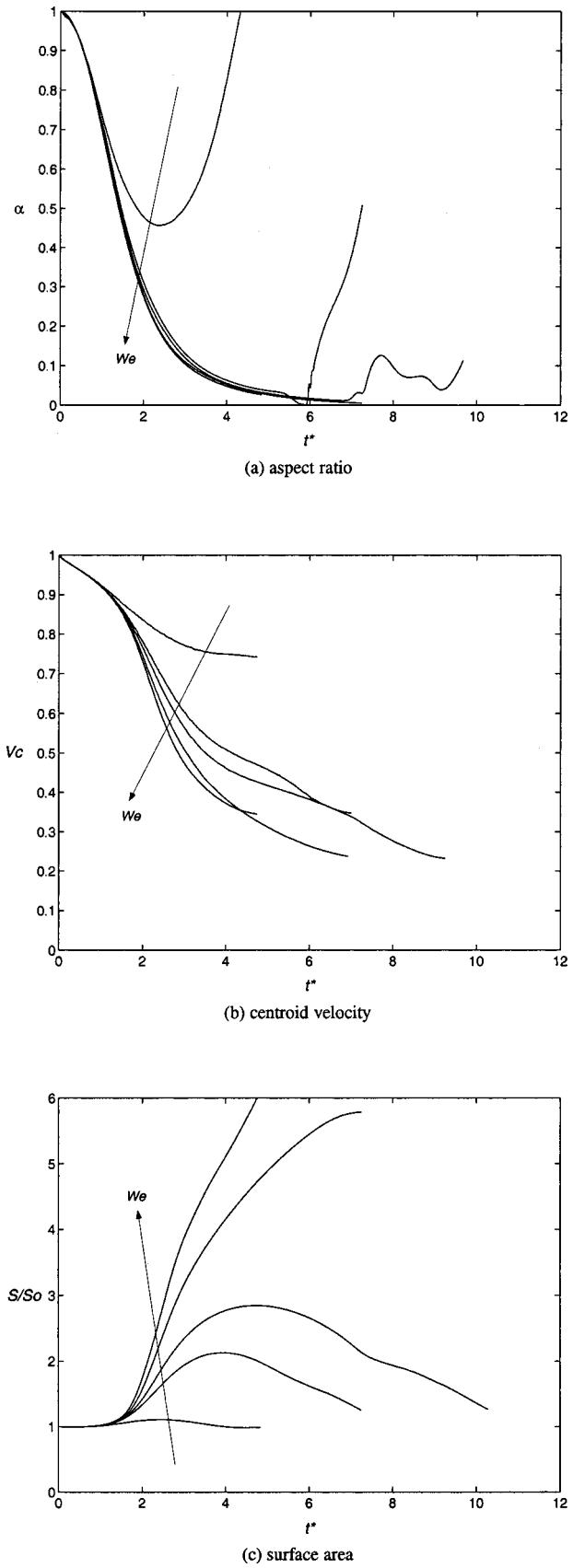

FIG. 5. Nondimensionalized aspect ratio, centroid velocity, and surface area plotted vs t^* for selected cases of the drops shown in Fig. 4. Results for five We=3.74, 12.5, 18.7, 37.4, and 93.5 are compared. $\rho_d/\rho_o=10$, Re=242, and $\mathrm{Re}_d=1935$.

moving faster than the rim and the bag faces the upstream direction). The drop with zero surface tension in (j) also displays a forward-facing bag. In this case small-scale irregularities are observed both on the edge and on the drop surface facing the downstream direction. This is due to the absence of surface tension, which suppresses the formation of the small-scale structures caused by the interfacial shear.

As the drops in Fig. 4 continue to deform, a thin film of drop fluid is formed in several cases. This film becomes very thin and eventually it is not resolved on the grid used. Although we have not performed a systematic study of how accurately the motion of the film is computed as the resolution is reduced, we believe that the motion is captured in a physically meaningful way. As the film becomes thin, its inertia is of much smaller importance than surface tension and even if the computation of inertia forces becomes inaccurate (since the mass has been spread over a distance much thicker than the film), surface tension is computed to the same level of accuracy as for an interface between two fluids. Since the film is clean, we would also expect viscous forces to be much smaller than surface tension.

A direct comparison of the above simulations with experiments in the same physical parameter range is not readily feasible due to the limited availability of experimental data on the secondary breakup at high pressure (small density ratios).[16] Among those available, an investigation by Gökalp *et al.*[24] is most relevant for comparison. They reduced the density ratio by increasing the pressure of the ambient gas at room temperature. Even though their lowest value of the density ratio ($\rho_d/\rho_o\approx 60$) is still higher than ours, similar transitions of the breakup modes are reported. Another study at elevated gas pressure with density ratios between 80 and 700 was done by Lee and Reitz.[25] At We=148 and 270, their photographs show a breakup mode similar to the forward-facing bag mode. They found, however, a breakup in the backward-facing bag mode at We=72, while our simulation shows a breakup in the forward-facing bag mode. This discrepancy is caused in part by the difference in the density ratio but, more importantly, by different loading history: A transverse gas jet is used in their experiment and the drop accelerates more gradually than in shock-tube experiments. As a result, the instantaneous value of the Weber number at the time of breakup should be much lower than the reported one.

The aspect ratio, centroid velocity, and surface area of some of the drops shown in Fig. 4 are plotted versus t^* in Fig. 5. The aspect ratio plot displays an oscillation of the drop with the lowest We and monotonic decrease for the other drops. When the drops with We=12.5 and 18.7 start to resume their initial shape, an abrupt increase in the aspect ratio is observed. The velocity plot shows a monotonic decline for all We shown. The surface area plot shows that the rate of deformation increases with We.

In Figs. 6 and 7, vorticity contours (left) and streamlines in a frame moving with the drop (right) are plotted along with the drop contour at selected times for the We=18.7 and We=93.5 drops shown in Figs. 4(c) and 4(i), respectively. In both cases, the vorticity plots show that most of the vorticity is created at the outer edge of the drop, as expected. The

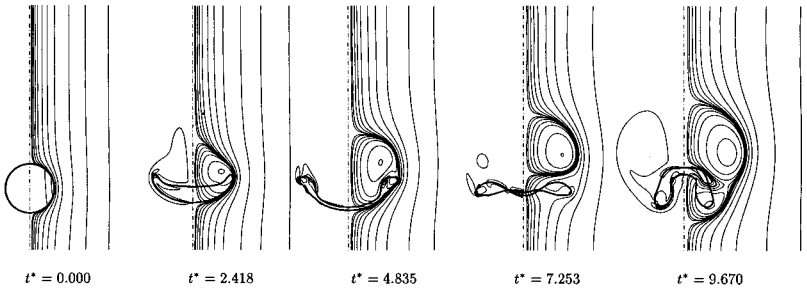

FIG. 6. Vorticity contours (left) and streamlines with a frame moving with the drop (right) plotted for the drop shown in Fig. 4(c).

streamline pattern for the We=18.7 drop shows that the backward-facing bag is stretched upward when the wake downstream of the drop detaches from it. On the other hand, the closed streamlines around the We=93.5 drop suggests that the drop moves as a vortex ring, forming a forward-facing bag.

Inviscid flow simulations using a vortex method with 400 point vortex rings are presented for We=93.5 and $\rho_d/\rho_o=10$ in Fig. 8. The evolution of three inviscid drops with different blob sizes, $\delta/D=0.03125$, 0.025, and 0.01875, are shown in (a), (b), and (c), respectively. In addition, the viscous simulation for the same Weber number and the density ratio—already shown in Fig. 4(i)—is illustrated again in (d) for comparison. In each column, the drop shapes are plotted every $t^*=0.4835$. Note that δ was introduced in Eq. (9) only to avoid singularity and that the choice of δ is somewhat arbitrary. The overall drop evolution is, however, not very sensitive to the exact value of δ: In all three cases, a thin film of drop liquid is pulled away from the shoulder of the main drop. Differences exist in the small scale structures, such as the thickness of the film which reduces faster for smaller δ. The viscous drop in (d) also displays an evolution similar to those of the inviscid drops.

The centroid velocities of the drops in Figs. 8(a)–8(d) are compared in Fig. 9. As the drops start moving, the viscous simulation shows a faster decrease of the initial velocity, compared to the inviscid results. Later, the inviscid drops deform more and the trend is reversed. As observed in Fig. 8, the rate of deformation of the inviscid drops increases slightly as δ is reduced. The velocity therefore decreases faster as δ decreases.

In spite of some differences, due to viscosity on the one hand and finite regularization on the other, the viscous drop and the inviscid ones display essentially the same behavior. Traditional ''shear''[3] or ''boundary-layer stripping''[5] breakup theories are based on the assumption that viscous boundary layers develop on both sides of the interface and viscous shear causes a portion of the drop fluid to be stripped from the drop shoulder. The validity of this assumption has been questioned by Lee and Reitz,[25] whose experimental observations in the shear breakup regime were independent of the Reynolds number, suggesting weak influence from the viscous boundary layers. As an alternative, they proposed a ''stretching–thinning'' type breakup mechanism where the thin edge of the drop, flattened by the aerodynamic pressure, is deflected in the downstream direction by blowing of the ambient fluid. Our inviscid simulations show that the initial formation of the thin film from the drop shoulder is an inviscid phenomenon, supporting the ''stretching–thinning'' type mechanism.

2. Evolution of drops with $\rho_d/\rho_o=1.15$

Figure 10 shows the deformation versus time of drops with a density ratio of 1.15 in the same way as in Fig. 4. The Weber numbers are 2.73, 13.7, 27.4, 54.7, and ∞; the Reynolds number is fixed at 331; and the drop-based Reynolds number is 381. The computations were done using a 128×256 grid. The low Weber number drop in (a) oscillates due to the high surface tension. As We is increased to 13.7 in (b), an indentation develops on the drop surface facing the downstream direction. Later, the momentum of the drop decreases and the surface tension causes it to oscillate. The drop shown in (c) for We=27.4 also deforms into an indented ellipsoid initially. The indentation deepens progressively and later meets the drop surface facing the upstream direction, forming a forward-facing bag as observed in part I for drops accelerated by a constant body force. However, since there is no driving force to sustain the deformation against the surface tension, the drop eventually resumes its initial shape. This is consistent with a statement made by Gel'fand.[16] For liquid–liquid systems with density ratios of $O(1)$, the bag and the transitional breakup modes are rarely observed experimentally for We$<$30. The drop with We=54.7 in (d), on

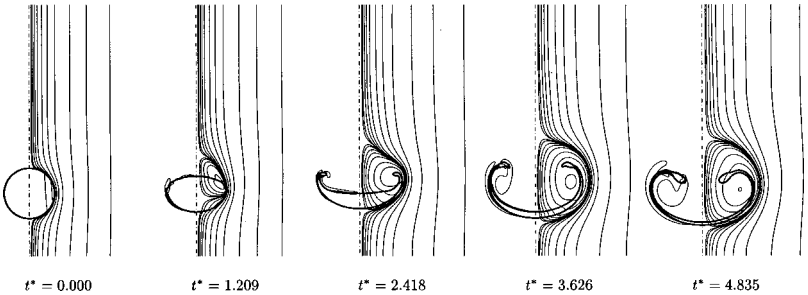

FIG. 7. Vorticity contours (left) and streamlines with a frame moving with the drop (right) plotted for the drop shown in Fig. 4(i).

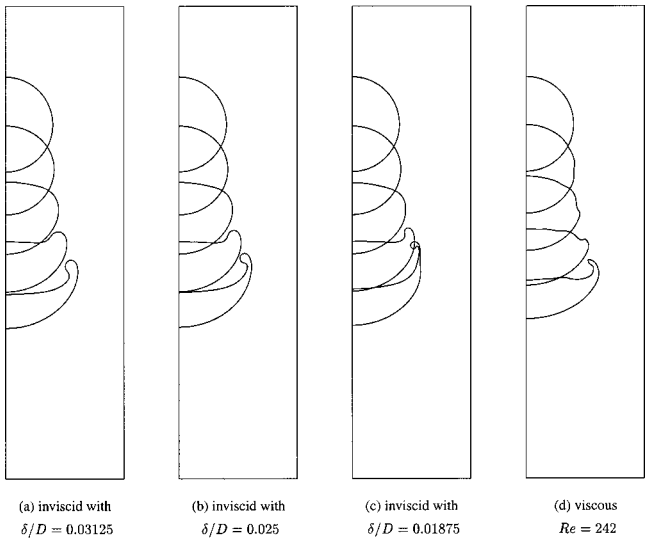

FIG. 8. Inviscid flow simulations for We=93.5 and $\rho_d/\rho_o=10$ with three different values of $\delta/D=0.03125$ (a); 0.025 (b); 0.01875 (c). In (d), the viscous result shown in Fig. 4(i) is included for comparison. The drop shapes are plotted every $t^*=0.4835$ in each column.

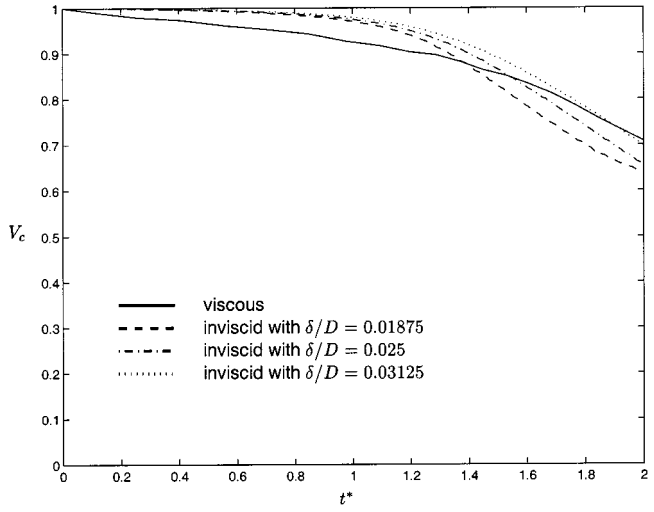

FIG. 9. Centroid velocities of the drops shown in Fig. 8 plotted vs t^*.

the other hand, shows increased initial deformation which results in a bigger rim that is connected by a forward-facing bag. For zero surface tension, (e), the drop displays a roll-up of the interface. A similar roll-up has been observed in the constant acceleration cases for drops with no surface tension.

In Fig. 11, the normalized aspect ratio, centroid velocity, and surface area are plotted versus t^* in (a)–(c), respectively, for the drops shown in Fig. 10. The aspect ratio plot shows shape oscillation for the two lower values of We. For higher We, the aspect ratio decreases monotonically to zero as the indentation deepens. The velocity plot in (b) shows a rapid decline initially. Later, the velocity of the drops with We=2.73 and 13.7 decreases but with fluctuations. After reaching a first minimum, the velocities of the drops with the three higher Weber numbers start to increase again when most of the drop fluid is in the torus-shaped rim and a very thin forward-facing bag is attached to it. Finally, they de-

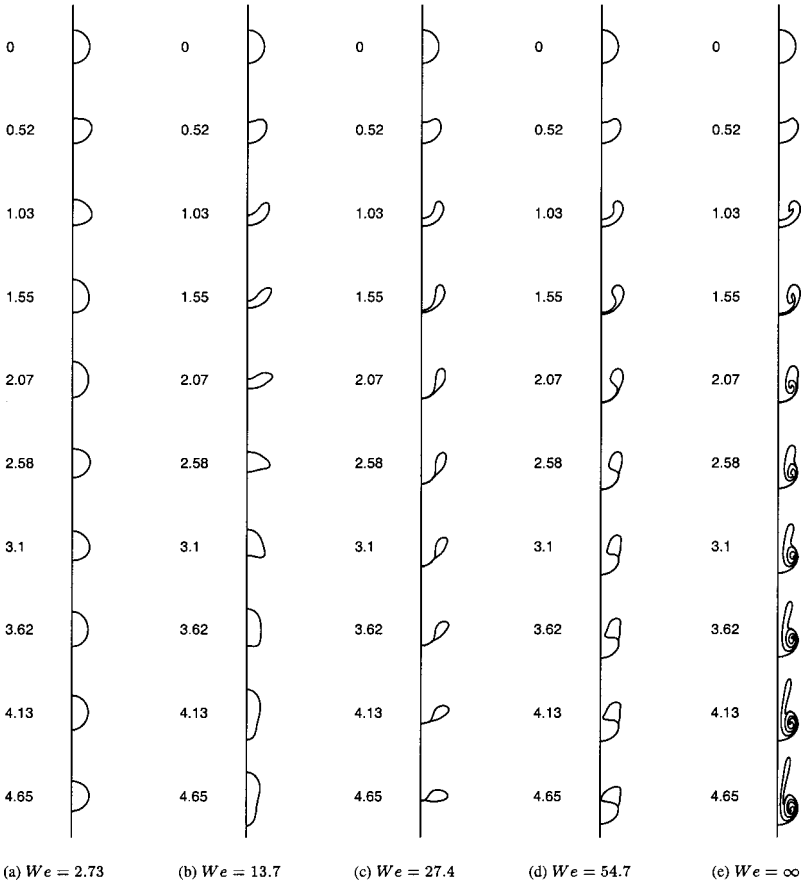

FIG. 10. Effect of We on the deformation of impulsively started drops with $\rho_d/\rho_o=1.15$, Re=331, and Re_d=381. The numbers inside the frames denote t^* when the interfaces are plotted. The computations were done on a 128×256 grid.

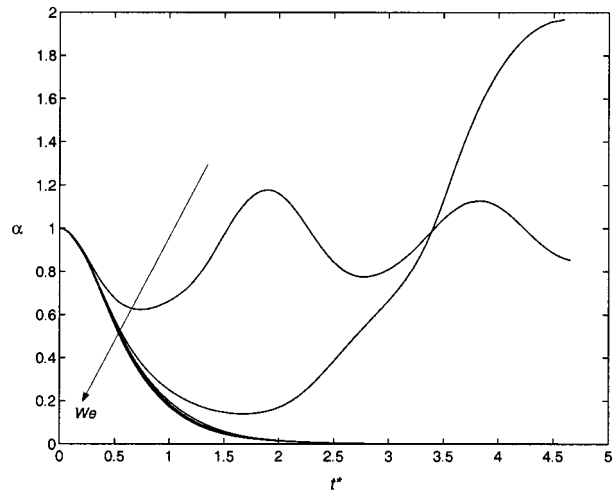

(a) aspect ratio

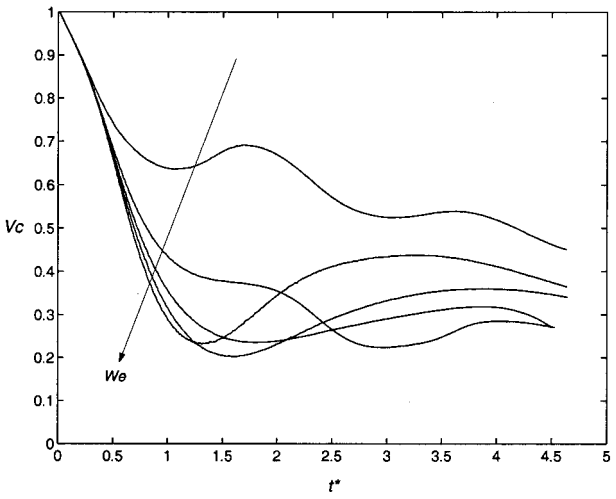

(b) centroid velocity

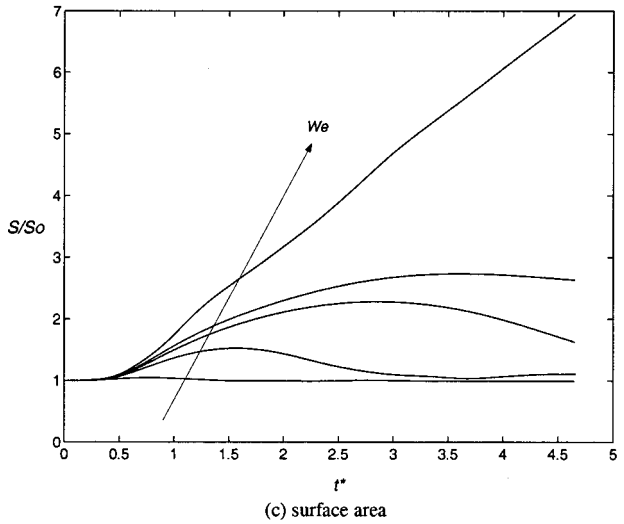

(c) surface area

FIG. 11. Nondimensionalized aspect ratio, centroid velocity, and surface area plotted vs t^* for the drops shown in Fig. 10. Results for five We $=2.73$, 13.7, 27.4, 54.7, and ∞ are compared. $\rho_d/\rho_o=1.15$, Re$=331$, and Re$_d=381$.

crease again as the drop deformation progresses. The surface area plot in (c) shows the effect of We on deformation: As We increases, the slope of the curve increases.

B. Effect of Re

In order to see the effect of the viscosity of the ambient fluid, simulations with four different Reynolds numbers, Re $=387$, 242, 121, 60.5 (from left to right) are compared in Fig. 12. In the top row (a), We$=18.7$, $\rho_d/\rho_o=10$, and Re$_d$ $=1935$. The overall evolution of the drops with two higher Reynolds numbers, Re$=387$ and 242, are very similar and the only difference is in the small-scale structure. The results for the two lower Reynolds numbers, Re$=121$ and 60.5, however, display some differences: Increasing the ambient fluid viscosity (decreasing the Reynolds number) while the other parameters are fixed can lead to a transition from the backward-facing bag mode to the oscillatory deformation mode. Another comparison is made in (b) for We$=74.8$, while the other parameters remain the same as in (a). Here, a transition from the forward-facing bag mode to the backward-facing bag mode is observed as the Reynolds number is reduced from 121 to 60.5.

Based on these observations, it is clear that as the Reynolds number is decreased, progressively higher Weber numbers are necessary in order to observe the same mode of deformation. The translation of the boundaries between different deformation modes—oscillation, backward-facing bag, and forward-facing bag—to higher We is clearly due to the increased viscous dissipation.

In Fig. 13, the surface areas of the drops shown in Fig. 12 are plotted versus the nondimensional time t^*. The comparison in (a) for drops with We$=18.7$ shows that the initial rate of increase of the surface area becomes higher as the Reynolds number increases. The same trend is confirmed for We$=74.8$ in (b).

C. Effect of Re$_d$

In Fig. 14, the effect of drop viscosity is shown for drops with $\rho_d/\rho_o=10$ and Re$=242$. The number in each frame denotes the dimensionless time when the drop is plotted. In the top row, four cases are compared for different drop viscosities (represented by the drop Reynolds number) at a fixed Weber number, We$=28.1$. As the drop viscosity is increased from left to right by an order of 10^3, the drop deformation is greatly reduced. The least viscous drop, with Re$_d=1935$, clearly shows the formation of a backward-facing bag, while the most viscous drop with Re$_d=1.935$ remains in an oblate shape. In the middle row, a similar comparison is made for We$=56.1$. Again, by increasing the drop viscosity, the drop deformation is reduced and the drop changes from a forward-facing bag to an oblate drop. The result for We$=93.5$ drops shown in the bottom row displays a similar trend.

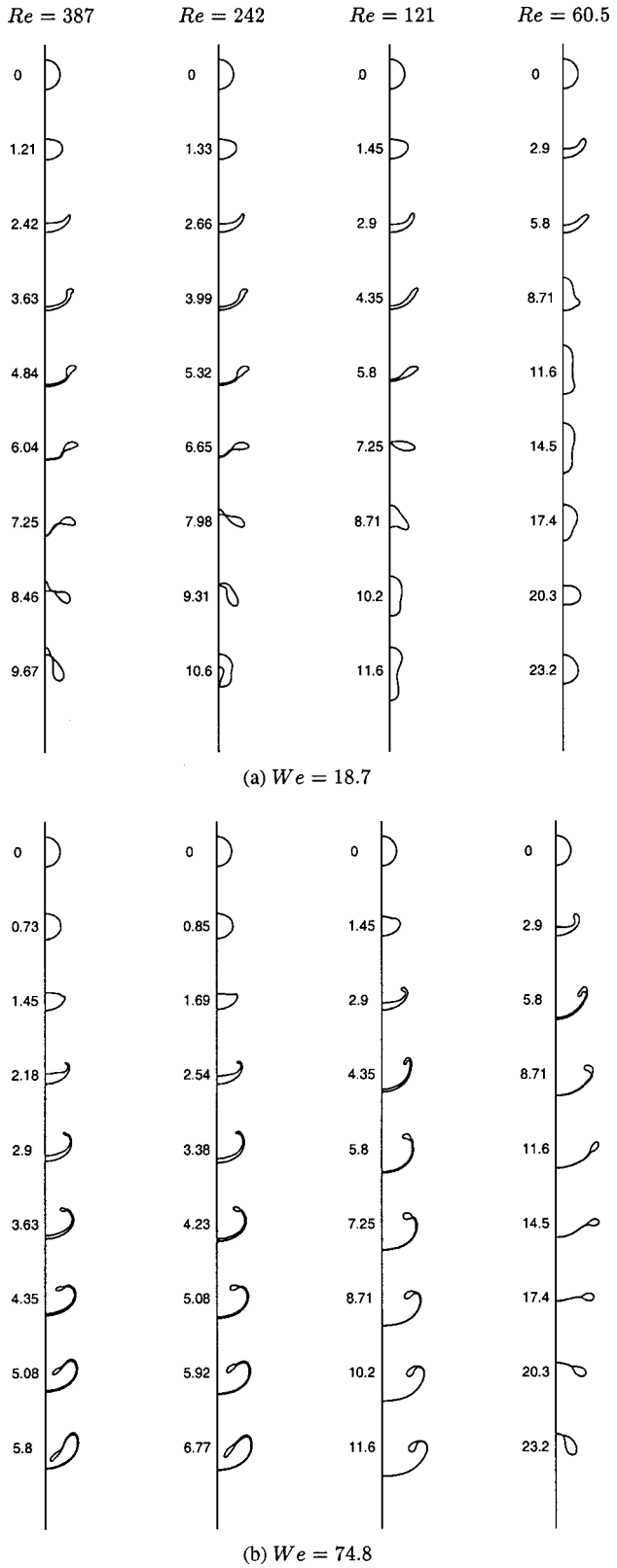

FIG. 12. Effect of the Reynolds number on the deformation of drops with $\rho_d/\rho_o=10$ and $\mathrm{Re}_d=1935$. In the top row (a), results with We=18.7 and four Reynolds numbers, Re=387, 242, 121, 60.5 (from left to right) are compared. In the bottom row (b), a similar comparison is made for We =74.8 with the same set of the Reynolds numbers. The numbers next to the drops denote t^* when the drop contours are plotted. The centroids of the drops in a column are separated by a fixed distance. The gap between two successive drops in a column does not represent the distance the drop travels during the time interval. The computations were done on a 256×512 grid.

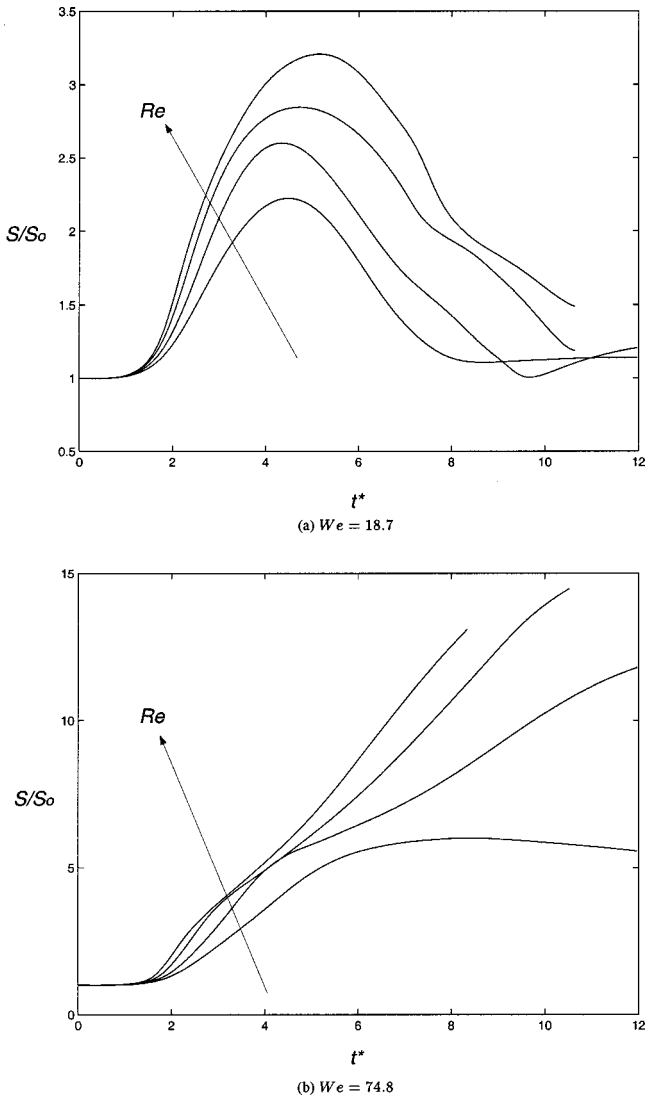

FIG. 13. Nondimensionalized surface area plotted vs t^* for the drops shown in Fig. 12. Results are compared for four Reynolds numbers, Re =60.5, 121, 242, and 387. In (a), results for the We=18.7 drops are presented and in (b), those for the We=74.8 drops are shown.

D. Deformation and breakup regime map

In Fig. 15(a), a breakup map is shown to summarize the deformation and breakup modes of drops with $\rho_d/\rho_o=10$ and $\mathrm{Re}_d=1935$. The horizontal and vertical axes represent the Reynolds number based on the ambient fluid properties and the Weber number, respectively. The various breakup modes are denoted by different symbols. When the Weber number is low, surface tension prevents large deformation so the drop only oscillates. As the Weber number increases past a critical value (approximately 16) for high Re, a backward-facing bag starts to emerge. When the Weber number is higher than approximately 30, the drops break up in a backward-facing bag mode for low Reynolds numbers and in a forward-facing bag mode at high Reynolds numbers. The transitions from the backward-facing bag mode to the forward-facing bag mode occur at progressively lower Weber numbers as the Reynolds number increases. As the Weber number is raised to 100, approximately, all drops break

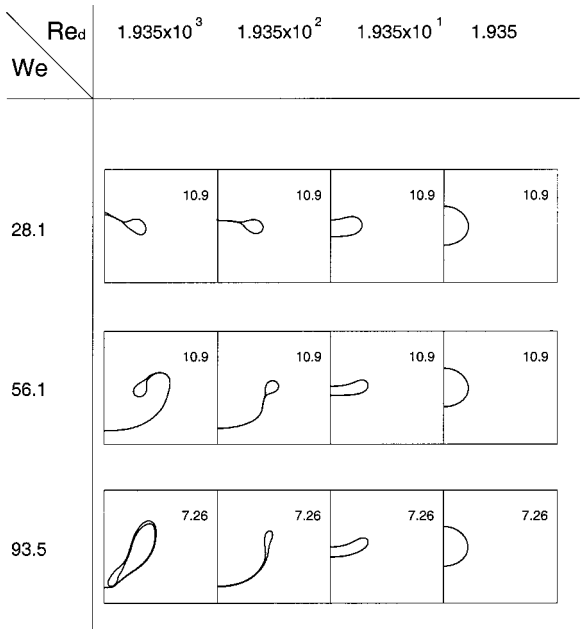

FIG. 14. Effect of the drop Reynolds number on the deformation of drops with $\rho_d/\rho_o=10$ and Re=242. The number in each frame denotes t^* when the drop is plotted.

up in the forward-facing bag mode for the Reynolds number range examined. Finally, when the surface tension vanishes (We$\rightarrow\infty$), the strong shear due to the outside flow peels off the drop interface and small irregularities on the drop surface are observed.

A similar breakup map is presented in Fig. 15(b) for the drops with $\rho_d/\rho_o=1.15$ and Re$_d$=1935. Again, when the Weber number is low, the drops only oscillate due to large surface tension. As the Weber number is increased, the backward-facing bag mode displayed in (a) for $\rho_d/\rho_o=10$ is no longer observed since the momentum difference between the drop and the ambient fluid is very small. Instead, the drops in this Weber number range recover their initial spherical shapes. When the Weber number is greater than 100, the drop deforms into a forward-facing bag and roll-up of the interface is observed. The effect of the Reynolds number is similar to what has been observed in (a): the boundaries between different deformation/breakup modes move to lower Weber numbers as the Reynolds number increases.

IV. CONCLUSIONS

To study the characteristics of impulsively accelerated drops, numerical simulations have been done for two density ratios, 1.15 and 10. These values of ρ_d/ρ_o are lower than those used in most experimental investigations of the drop breakup due to impulsive disturbance and therefore are more relevant to high pressure sprays. At low We (<10), the drops display oscillatory deformation. As We increases, an indentation develops on the drop surface facing the downstream direction. Since the velocity and the aerodynamic forces causing deformation continue to decrease, the surface tension eventually takes over and the drops resume the initial spherical shape.

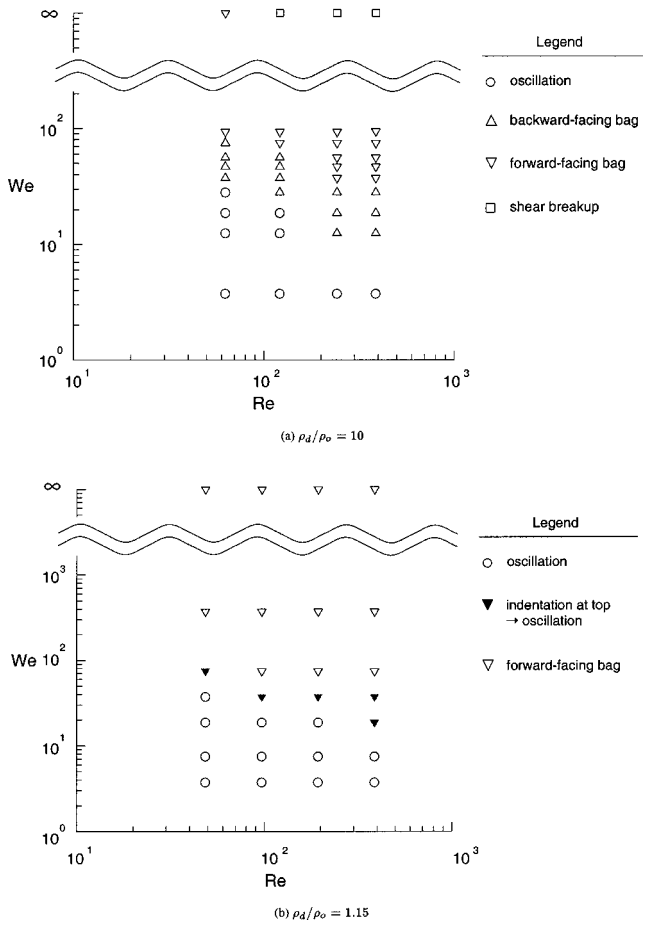

FIG. 15. Breakup mode maps for impulsively started drops with Re$_d$ =1935. The density ratios are 10 and 1.15 in (a) and (b), respectively.

The formation of a backward-facing bag is seen only for the larger density ratio (10), which is consistent with experimental observations indicating that this type of breakup is rarely observed for liquid–liquid systems.[16] Our finding also supports the general observation in previous studies using impulsive acceleration—the disruptive aerodynamic force must be imposed for a sufficiently long time for the formation and the growth of a backward-facing bag (for example, see Ref. 26). The present simulations show that the velocity decreases too fast when the density ratio is close to one. Therefore, flow separation and the appearance of the wake behind the drops (the physical mechanism of a backward-facing bag formation as proposed in the case of continuously accelerating drops[1]) are not likely to be sustained.

When We is further increased, the initial deformation is so large that a forward-facing bag is formed. This is found to be an inviscid phenomenon, confirmed by inviscid flow simulations showing essentially the same development of a thin film of drop liquid drawn from the drop shoulder in the downstream direction. In the case of vanishing surface tension, small-scale irregularities develop on the drop contour, similar to experimental observations of liquid drops in gas flows at very high We.

ACKNOWLEDGMENTS

This effort was sponsored by the Air Force Office of Scientific Research, Air Force Material Command, USAF,

under Grant Nos. F49620-96-1-0356 and F44620-99-1-0314. The U.S. Government is authorized to reproduce and distribute reprints for Governmental purpose notwithstanding any copyright notation thereon. The views and conclusions contained herein are those of the authors and should not be interpreted as necessarily representing the official policies or endorsements, either expressed or implied, of the Air Force Office of Scientific Research or the U.S. Government. Some of the computations were done using the facilities of the Center of Parallel Computing at the University of Michigan and those at the NAV-OCEANO DoD MSRC.

[1]J. Han and G. Tryggvason, ''Secondary breakup of axisymmetric liquid drops. I. Acceleration by a constant body force,'' Phys. Fluids **11**, 3650 (1999).
[2]W. R. Lane, ''Shatter of drops in streams of air,'' Ind. Eng. Chem. **43**, 1312 (1951).
[3]J. O. Hinze, ''Fundamentals of the hydrodynamic mechanism of splitting in dispersion process,'' AIChE J. **1**, 289 (1955).
[4]A. R. Hanson, E. G. Domich, and H. S. Adams, ''Shock tube investigation of the breakup of drops by air blasts,'' Phys. Fluids **6**, 1070 (1964).
[5]A. A. Ranger and J. A. Nicholls, ''Aerodynamic shattering of liquid drops,'' AIAA J. **7**, 285 (1969).
[6]B. E. Gel'fand, S. A. Gubin, S. M. Kogarko, and S. P. Komar, ''Singularities of the breakup of viscous liquid droplets in shock waves,'' J. Eng. Phys. **25**, 1140 (1973).
[7]S. A. Krzeczkowski, ''Measurement of liquid droplet disintegration mechanisms,'' Int. J. Multiphase Flow **6**, 227 (1980).
[8]A. A. Borisov, B. E. Gel'fand, M. S. Natanzon, and O. M. Kossov, ''Droplet breakup regimes and criteria for their existence,'' J. Eng. Phys. **40**, 44 (1981).
[9]R. D. Reitz, and F. V. Bracco, ''Mechanism of breakup of round liquid jets,'' in *Encyclopedia of Fluid Mechanics* (Gulf, Houston, TX, 1986), Vol. 3.
[10]M. Pilch and C. A. Erdman, ''Use of breakup time data and velocity history data to predict the maximum size of stable fragments for acceleration-induced breakup of a liquid drop,'' Int. J. Multiphase Flow **13**, 741 (1987).
[11]A. Wierzba, ''Deformation and breakup of liquid drops in a gas stream at nearly critical Weber numbers,'' Exp. Fluids **9**, 59 (1990).
[12]L.-P. Hsiang and G. M. Faeth, ''Near-limit drop deformation and secondary breakup,'' Int. J. Multiphase Flow **18**, 635 (1992).
[13]L.-P. Hsiang and G. M. Faeth, ''Drop properties after secondary breakup,'' Int. J. Multiphase Flow **19**, 721 (1993).
[14]L.-P. Hsiang and G. M. Faeth, ''Drop deformation and breakup due to shock wave and steady disturbances,'' Int. J. Multiphase Flow **21**, 545 (1995).
[15]D. D. Joseph, J. Belanger, and G. S. Beavers, ''Breakup of a liquid drop suddenly exposed to a high-speed airstream,'' Int. J. Multiphase Flow **25**, 1263 (1999).
[16]B. E. Gel'fand, ''Droplet breakup phenomena in flows with velocity lag,'' Prog. Energy Combust. Sci. **22**, 201 (1996).
[17]H. Liu, *Science and Engineering of Droplets* (William Andrew, Norwich, NY, 2000), p. 169.
[18]R. I. Nigmatulin, *Dynamics of Multiphase Media 1* (Hemisphere, New York, 1991), pp. 150–163.
[19]J. B. Heywood, *Internal Combustion Engine Fundamentals* (McGraw-Hill, New York, 1988), p. 522.
[20]S. O. Unverdi and G. Tryggvason, ''A front-tracking method for viscous, incompressible, multi-fluid flows,'' J. Comput. Phys. **100**, 25 (1992).
[21]G. Tryggvason, B. Bunner, O. Ebrat, and W. Tauber, ''Computations of multiphase flows by a finite difference/front tracking method–I. Multi-fluid flows,'' 29th Computational Fluid Dynamics, von Karman Institute for Fluid Dynamics Lecture Series 1998-03 (1998).
[22]W. J. A. Dahm, C. M. Scheil, and G. Tryggvason, ''Dynamics of vortex interaction with a density interface,'' J. Fluid Mech. **205**, 1 (1989).
[23]M. Abramowitz, *Handbook of Mathematical Functions, with Formulas, Graphs, and Mathematical Tables* (Dover, New York, 1973).
[24]I. Gökalp, C. Chauveau, C. Morin, B. Vieille, and M. Birouk, ''Improving droplet breakup and vaporization models by including high pressure and turbulence effects,'' Atomization Sprays **10**, 475 (2000).
[25]C. H. Lee and R. D. Reitz, ''An experimental study of the effect of gas density on the distortion and breakup mechanism of drops in high speed gas stream,'' Int. J. Multiphase Flow **26**, 229 (2000).
[26]S. S. Sadhal, P. S. Ayyaswamy, and J. N. Chung, *Transport Phenomena with Drops and Bubbles* (Springer-Verlag, New York, 1996).